A gas microstrip detector for XAS studies in the photon energy region 300–1500 eV

J. D. Lipp,[a]* J. E. Bateman,[a] G. E. Derbyshire,[a] I. W. Kirkman,[b] G. van der Laan,[b] R. Stephenson[a] and C. M. Teodorescu[b]

[a]CCLRC Rutherford Appleton Laboratory, Chilton, Didcot OX11 0QX, UK, and [b]CCLRC Daresbury Laboratory, Daresbury, Warrington WA4 4AD, UK. E-mail: j.lipp@rl.ac.uk

The ability to perform X-ray absorption spectroscopy (XAS) in the 300–1500 eV energy range allows measurements to be made on transition metal compounds. This paper describes a detector and the technique used to perform fluorescent measurements on such materials. A variety of test sample results are shown to illustrate the low energy and energy-resolving capabilities of the detector (based on gas microstrip technology). Two possible applications are also demonstrated. The first shows how the detector can be used to gather X-ray absorption spectra for the *L* edges of transition metals and *K* edges of light elements (C, O and N). The other shows how the magnetic immunity of the detector can be exploited to study the magnetic properties of materials.

Keywords: gas microstrip; soft X-ray detectors; XAS; X-ray magnetic circular dichroism.

1. Introduction

The use of sub-keV X-rays is opening up important fields of study. The ability to perform analysis on the carbon and oxygen *K* edges typically found in biological samples would be a useful addition to the tools currently available. 3*d* transition metal elements, whose *L* edges are in this energy region, have a number of important properties, being the basis for many modern technologies. A review of the range of techniques involved is found in Koningsberger & Prins (1998) and Stohr (1992). *L*-shell XAS studies of 3*d* transition metal elements have also recently been developed for the study of magnetic properties using X-ray magnetic circular dichroism (van der Laan & Thole, 1991).

Instrument developments in the X-ray region, below 1 keV, permit the study of such atoms by probing the *L* shells of the more dense elements and also the study of their environment by probing the *K* shell of the O atoms in their oxides. Such studies may be carried out using total electron yield, but this technique is inherently surface sensitive and becomes less useful for insulating samples. An alternative, the transmission method, is achievable but samples must be of the order of a few nanometers thick to be of use in the sub-keV region. In practice, producing such samples, which have to be pinhole-free, is so difficult that it cannot be done routinely. Studies based on measuring the fluorescent yield of the sample (Fischer *et al.*, 1989) are relatively insensitive to surface effects, can be used with insulating samples and do not require the painstaking preparation that limits the use of transmission samples. However, the fluorescent yield of *L* shells and *K* shells is very low in this energy region (less than 1%) and so any measurement system based on fluorescence photons must be sensitive and have a high degree of immunity to noise.

Since their invention, gas microstrip detectors (GMSDs) (Oed, 1988) are finding increasing applications in the synchrotron radiation environment. Recent developments at Rutherford Appleton Laboratory have resulted in GMSD systems capable of measuring X-rays in the sub-keV region. The ability to tune their characteristics by varying the fill gas and the possibility of generating very high gas gains means that demanding noise floor specifications can be met. GMSDs are well suited to fluorescence measurements and have already been utilized in this way (Smith *et al.*, 2001; Bateman *et al.*, 2001*a*).

Previous work has demonstrated that it is possible to operate a GMSD in a strong magnetic field (Bateman *et al.*, 2001*b*). This provided a unique tool for making measurements of the magnetic properties of materials using the technique of X-ray magnetic circular dichroism (XMCD) (van der Laan & Thole, 1991). The prototype detector suffered some limiting factors in operation, meaning that its noise floor and counting rates were both restricted. A custom design of the detector plates has resulted in a detector with a higher efficiency and lower noise floor than the prototype, which is suited to wider application than just the magnetic studies originally intended. This paper demonstrates how such a detector system has been developed to make XAS of 3*d* transition metal *L* edges and low-atomic-number element *K* edges possible. Results of the detector characterization together with some sample XAS scans are presented.

Other existing detector technologies such as lithium-drifted silicon [Si(Li)], silicon drift detectors and high-purity germanium (HPGe) detectors are also capable of sensing X-rays in the sub-keV region. In most cases, however, these use long shaping times thus reducing their maximum event rates and require cooling with liquid nitrogen making regular maintenance of the nitrogen supply essential. These technologies are also limited in application owing to the fact that they are not immune to strong magnetic fields.

2. Detector and counting system

The detector, which is shown graphically in Fig. 1 of Bateman *et al.* (2001*b*), consists of a stainless steel tube of diameter 30 mm and length 280 mm in which is mounted, on the central axis of the tube, a back-to-back pair of GMSD plates with the electrode pattern shown in Fig. 1. The direction of the electrode strips is parallel to the axis of the detector tube. This gives a detection area of approximately 12 mm $\times$ 12 mm which views the X-ray target through a MOXTEK polymer window of diameter 11 mm. The X-rays, which are nominally propagating parallel to the plates, interact with the gas above the electrodes after passing through a dead layer of gas near the entrance window. The detector body houses the low-noise preamplifiers and high-voltage distribution networks necessary for counter operation.

The new GMSD electrode design consists of two groups of 11 anodes and associated cathodes placed on a sheet of 1 mm-thick Schott S8900 glass (Fig. 1). All the contacts to the biasing and readout electronics are situated at one end of the plate. This keeps the other

Figure 1
Drawing of the electrode pattern used for this detector.

end of the plate free from relatively bulky contacts that would otherwise contribute to a dead region of detector through which X-rays would have to propagate in order to be detected. The active area of each group of electrodes has also been doubled to 26 mm long by 6 mm wide, again improving the efficiency of the detector.

The second improvement has been to tune the geometry of the anodes and cathodes so as to maximize the gain of the detector and hence increase the noise floor of the device (Mir *et al.*, 2002). The dimensions selected are cathodes of width 300 μm and anodes of width 5 μm, on a pitch of 500 μm.

The overall geometry of the detector vessel has not changed from that of the prototype (Bateman *et al.*, 2001*a*,*b*), but some improvements have been made to the biasing arrangement to enable greater flexibility and control over the bias potentials. Two high-voltage feedthroughs have been incorporated in the vessel flange, allowing both the anode and cathode potentials to be controlled independently. The capability to separate all four groups of electrodes has been added by allowing four signals to be taken out through the flange. It should be noted though, that for the experiments described the signals are paralleled through only two preamplifiers (each glass plate has its two anode groups paralleled together and connected to a single preamplifier). Each preamplifier is equipped with a CR-RC shaping amplifier at its output. For the results presented here, a shaping time of 1.5 μS is selected, though shaping times of 100 nS or faster are also possible if higher rates are required.

From the shaping amplifiers, the signal is fed into two separate readout channels. The first is a fast Comtec multi-channel analyser (MCA) which captures a pulse height (PH) spectrum from whichever detector channel is selected. The second parallel data channel consisted of an Ortec 473A discriminator on each detector channel, enabling a lower threshold of detection to be set. The outputs of these were then combined into a single Hytec scalar, which was read out by the station control computer, enabling the recording of count rates at each beam energy point during an experimental scan.

3. Experiment configuration

All the data presented in this paper were collected at Station 1.1 of the Synchrotron Radiation Source (SRS), Daresbury, UK. This beamline is equipped with a spherical grating, coated in nickel to provide harmonic rejection. Special attention was paid to the higher harmonic content of the incident photon beam, since the detector efficiency increases strongly with the X-ray energy. This particular grating has been characterized to energies as low as 400 eV making its performance known for most of the measurements described later. The carbon results are the exception and so no attempt has been made to collect a carbon XAS scan. Extending the grating characteristic curves suggests that the second harmonic does become significant, but does not exceed 10% at the carbon edge. The available flux varies with energy, with its maximum occurring at 770 eV. At 350 eV it is approximately 10%, and at 250 eV it is less than 1% of the maximum. The monochromator bandwidth is insignificant for all measurements, being less than 0.6 meV full width at half-maximum at the energies of interest.

An additional grating baffle in the beamline selects circularly polarized light (85%). It is removable to allow the use of predominantly linear polarized light (97%). Removal of the baffle gives an increase of approximately a factor of three in the photon flux at the sample.

The sample of interest, when solid, was mounted on a conductive substrate using a screw-down copper clamp. In the case of powder samples, the grains of powder were pressed into a piece of conductive double-sided tape, which in turn was stuck to the sample holder substrate. Space for numerous samples is available on the sample holder. The sample holder was then suspended on a linear and rotational manipulator inside the 'flipper' experimental vessel (Dudzik *et al.*, 2000). The samples were aligned at 45° to the incident beam, with the fluorescence detector mounted with its axis at 90° to the incident beam, looking at the illuminated spot on the sample at a radius of approximately 25 mm. The X-ray absorption-induced photoemission electron current signal was measured using a picoammeter with its input attached to the sample holder's conductive substrate.

Table 1
Materials used as test samples for experiments.

Name	Description
Sample-Co	Powder of Co_2TiO_4 pressed into graphite-impregnated tape
Sample-Fe	Magnetite (Fe_3O_4) powder pressed into graphite-impregnated tape
Sample-C	Graphite-impregnated STR tape from Shinto Paint
Sample-Cu	Solid block of copper (the sample holder substrate) with air oxidized surface layer
Sample-Ga	Substrate of GaAs, with ~40 monolayers of Fe grown on its surface; a 30 Å capping layer of copper was placed on top to protect the sample

4. Performance of the X-ray detector

To be detected, X-rays enter the detector through a thin vacuum-compatible polymer entrance window (Moxtek AP1.7). They then pass through a 5 mm region of dead gas before entering the active region of the detector. Fig. 2 shows the calculated detector efficiency curve obtained by combining the effects of the entrance window, the 'gas window' and the active length of the plate. It has been calculated for the gas mix used in all experiments in this report, 10% isobutane in helium. No correction is incorporated for angular variance in efficiency of the entrance window as this is considered irrelevant to the described experiments throughout which the geometry is kept constant.

A variety of samples consisting of materials of interest were available (Table 1). For conciseness, they will be referred to by their name throughout the remainder of this paper.

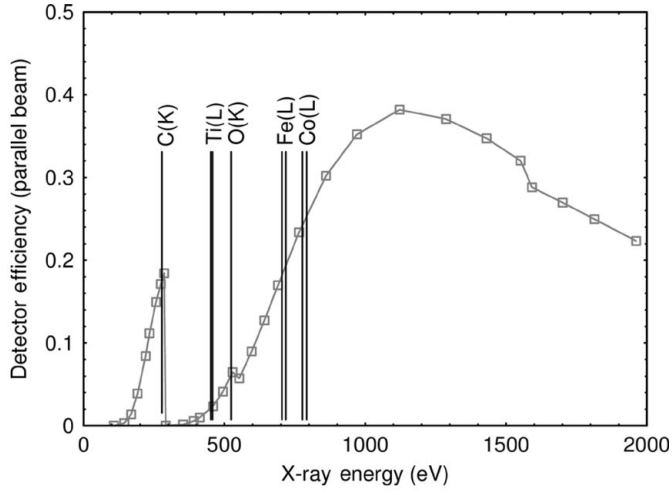

Figure 2
Model of the detector efficiency using 10% isobutane in He as the fill gas with the MOXTEK polymer window, assuming a parallel beam. The main *K* and *L* emission lines of interest are highlighted.

In order to establish the behaviour of the detector at low energy, PH spectra have been gathered for a variety of samples with fluorescence lines in the range 250–1100 eV.

The first data set presented in Fig. 3 shows how it is possible to obtain a clean X-ray line from a compound sample (Sample-Co). Fluorescent X-rays are recorded for incident energies just below (760 eV) and just above (782 eV) the L_3 edge (776.2 eV) of cobalt. The difference between the two spectra removes all the events, which are the result of secondary processes, such as backscattering, Compton scattering and events initiated by the harmonics that bleed through the monochromator. It is assumed that the magnitude of these secondary processes does not vary significantly between the two incident energies and hence their contribution can be removed by taking the difference. The resulting difference signal is therefore the true response of the detector to the Co L_α emission line.

The resulting difference spectrum in Fig. 3 is fitted to a lognormal distribution in Fig. 4. The form

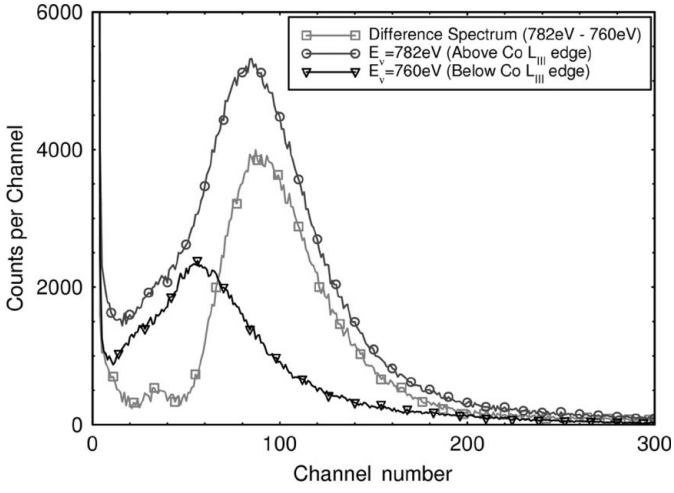

Figure 3
Detector PH spectra for Sample-Co excited at X-ray energies of 760 and 782 eV, respectively. The difference spectrum of the line of interest is also shown.

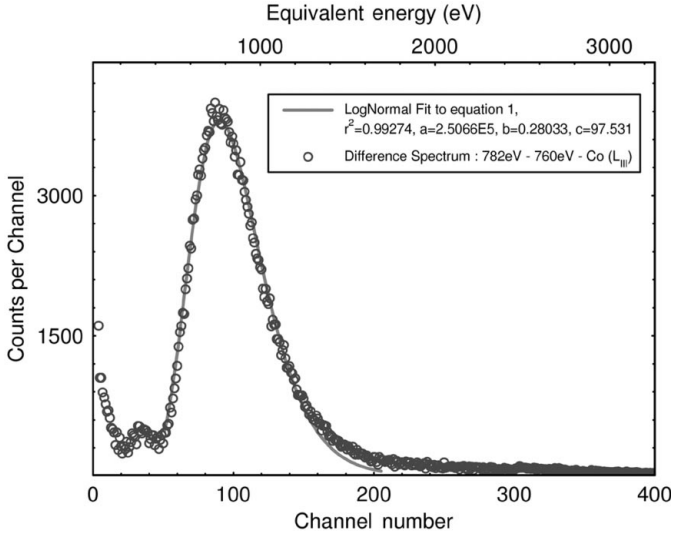

Figure 4
A lognormal fit is made to the subtracted Co line calculated in Fig. 3.

$$y = \left[\frac{a}{bx(2\pi)^{1/2}}\right]\exp\left\{\frac{-[\ln(x)-\ln(c)]^2}{2b^2}\right\} \quad (1)$$

is used where a is the integral of all the events in the measured line, b is the relative standard deviation (SD) of the detector response (actually the fractional SD of the normal distribution which results when the PH spectra is transformed to log space) and $\ln(c)$ is the mean of the distribution in log transform space. Previous results have shown this to be a valid and convenient fitting method (Bateman, 2002*b*). The peak of the fit may be found by setting the derivative of (1) to zero, yielding the result that the peak position is $c\exp(-b^2)$. It can be seen that the fit is good over the peak itself, but there is some distortion to either side. The distortion to the left of the main peak originates from partially collected events and there may also be a contribution from C in the sample holder. The long tail at energies higher than the Co peak is believed to result from a combination of harmonic contamination of the incident beam, the non-ideal drift electrode (owing to space constraints within the vessel), and event pile-up owing to the long shaping time used in the pulse readout.

Attempts to collect spectra from the titanium lines emitted from the same sample proved futile. This was expected, as the calculated efficiency of the detector around 450 eV is only 2% and, when combined with the very low fluorescence yield, the signal was almost non-existent.

It is also feasible to make the lognormal fit embrace two overlapping emission lines. This is clearly demonstrated using Sample-Fe, and Fig. 5 shows the PH spectrum collected for this sample while illuminated with 711.7 eV circularly polarized X-rays. The line fitted to the spectrum is the sum of two lognormal fits, one for the O line and the other for the Fe line,

$$y = \frac{a}{bx(2\pi)^{1/2}}\exp\left\{\frac{-[\ln(x)-\ln(c)]^2}{2b^2}\right\} + \frac{d}{gx(2\pi)^{1/2}}\exp\left\{\frac{-[\ln(x)-\ln(f)]^2}{2g^2}\right\}. \quad (2)$$

A good approximation to the energy and intensity of each line may be obtained from the parameters of the fit.

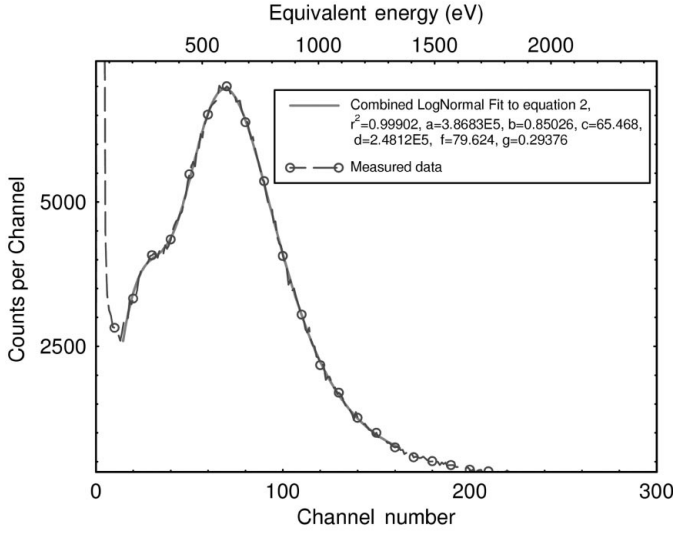

Figure 5
PH spectrum collected from Sample-Fe, incorporating Fe L_α and O K lines. A combined lognormal fit is overlaid on the actual data.

A similar process is completed for the PH spectrum collected from Sample-C, excited with 350 eV X-rays shown in Fig. 6. It should be noted that the beamline configuration prevented excitation at lower energies and hence the oxygen present in the tape was also excited by the second harmonics, which are estimated to be >5% of the incident beam. The lognormal fitting procedure has been applied only to the region around the C peak. The experiment has also been repeated to yield fits for Cu L_α using Sample-Cu and Ga L_α using Sample-Ga.

The channel positions obtained from all the lognormal fits are collated and plotted against the known edge energies for the X-ray emission lines in Fig. 7. The resultant calibration curve shows that all the pulse-height peak channels sit close to the straight-line fit, thus confirming that the detector and fitting procedures are operating in a linear manner. Likewise, in Fig. 8 the relative standard deviation (*b* parameter) from the fits is plotted and compared with measurements for a wall-less GMSD (Bateman, 2002*a*). The actual values obtained from these results are noticeably worse than is possible, owing to the compromises in the detector design necessitated by the space constraints and the requirement for high magnetic field tolerance.

The noise floor, defined by a total counting rate of 10 Hz in absence of X-rays, is less than 30 eV, which is sufficient to detect individual photoelectrons.

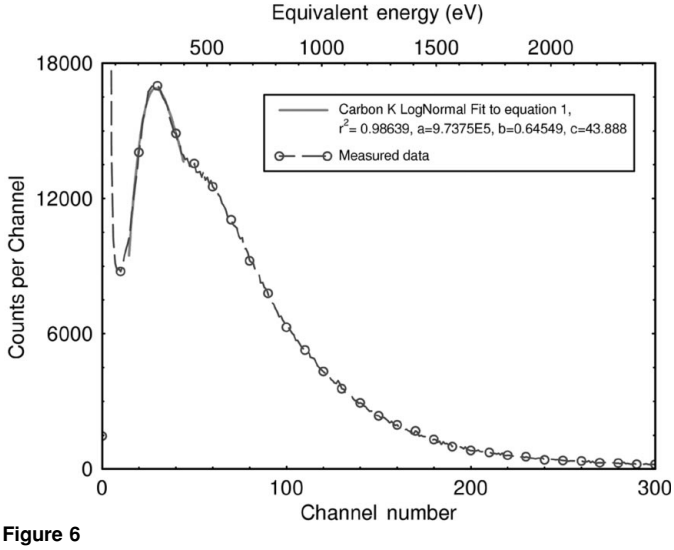

Figure 6
PH spectra collected from Sample-C. A lognormal fit is shown for the C line. The oxygen and nitrogen within the tape have also been excited by beam harmonics and appear as a bump on the high-energy side of the carbon line.

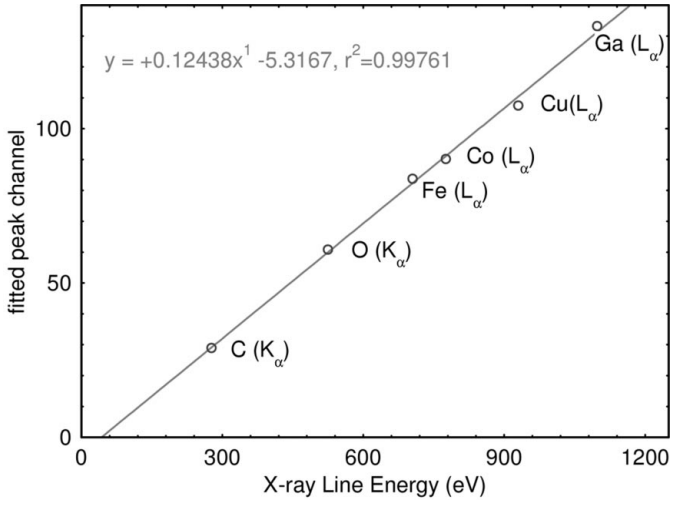

Figure 7
Calibration curve for the detector, combining the data sets collected in the previous figures and those collected for the Cu in Sample-Cu and the Ga in Sample-Ga.

5. X-ray absorption spectra

Having established the manner in which the detector behaves, some XAS spectra have been collected from the various samples. These were not intended as a primary outcome of the experiment conducted and hence they do not continue to high enough energies to allow full spectral analysis. However, they are still useful demonstrations of the effectiveness of the detector for low-*Z* atomic species.

Spectra were collected with the incident beam linearly polarized and aligned on Sample-Co. The results presented are collected using the discriminator-scalar readout channel. Both the sample and beam positions were held constant during the scans, with only the incident energy being varied. The discriminator lower threshold was selected such that the dark noise of the system was 1–2 Hz.

Scanning the incident energy over the Co L_3 (778.1 eV) and L_2 (793.2 eV) lines yields the fluorescence response shown in Fig. 9. The low fluorescent yield of the Co *L* shell is evident from the low count rate (2 kHz above background) and the noise in the curve corresponds to the statistical Poisson noise expected when integrating for 4 s at such a rate (1.1%).

Fig. 10 shows the result of scanning over the oxygen *K* edge in the same sample (520–550 eV).

6. X-ray magnetic circular dichroism

XMCD is one particular application of the detector, which permits the study of the magnetic properties of 3*d* transition metal elements. The technique involves measuring the X-ray absorption spectra for the sample of interest under applied magnetic field. The measurements are repeated for both helicities of the circularly polarized light and the difference signal is known as the dichroism. For reasons connected to beam stability (Dudzik *et al.*, 2000), an alternative and more convenient method involves using the same light polarization

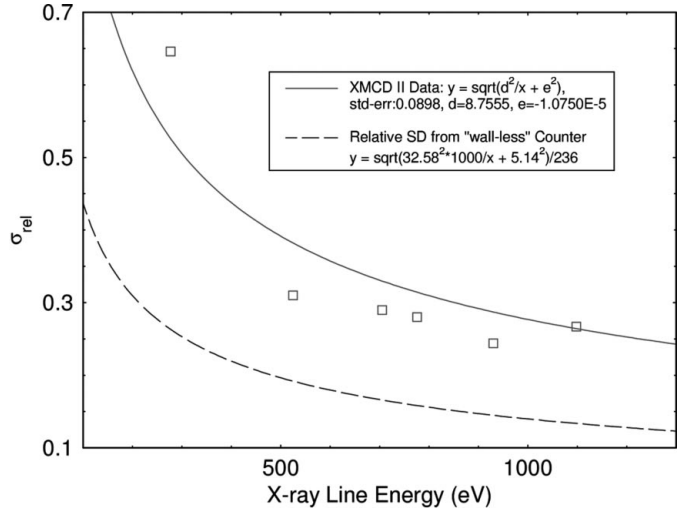

Figure 8
Relative standard deviation of the energy resolution of the detector (σ_{rel}) in log-space compared with the optimum obtained from a wall-less GMSD design (Bateman, 2002*a*).

but switching the direction of the magnetic field. The latter approach is used for the results presented here.

XAS scans were collected over the Fe L_3 and L_2 edges for Sample-Ga. The scans for each direction of the magnetic field are shown in Fig. 11. Also shown is the dichroism, obtained as the difference between the scans collected at opposite magnetic fields (± 0.5 T). When compared with the simultaneously measured total electron yield some differences are noted (Bateman *et al.*, 2001*b*). Firstly, because the fluorescence detector is immune to the magnetic field and the leakage current measurements are not, the corrections which need to be applied to the leakage measurements are not required. There is also a difference in the ratio of the peak heights (L_2/L_3). Finally, the XMCD signal has an extra feature between its positive and negative regions. Each of these differences provides a focus for further research.

In practice, these differences mean that the application of the XMCD sum rules to the spectrum obtained in fluorescence yield result in an unusually high Fe magnetic moment (2.7 μ_B instead of 1.9 μ_B, as measured in total electron yield). This discrepancy finds its origin in a variety of reasons, such as self-absorption, different selection rules (van Veenendaal *et al.*, 1996), core hole decay and experimental geometry. The fluorescence yield is thus not proportional to the absorption cross section. In order to interpret the XMCD data and to calculate the magnetic moments using the sum rules, it is necessary to correct the measured signal. This problem is beyond the scope of the present paper.

A further application exploiting the magnetic insensitivity of the detector is to measure magnetic hysteresis curves for a sample of interest. This technique involves illuminating the sample with circularly polarized X-rays at a fixed energy near the maximum of the XMCD, while stepping the magnetic field through a full hysteresis cycle. The absorption and fluorescence signals are recorded at each field value. Fig. 12 shows the hysteresis curve collected by fluorescence with Sample-Ga illuminated on the Fe L_3 edge. Again, a comparison between the two methods shows the fluorescence measurement to have advantages over the electron yield measurement. Leakage current measurements always need to undergo significant correction, owing to their distortion in magnetic fields, before they resemble a hysteresis curve. The fluorescence data

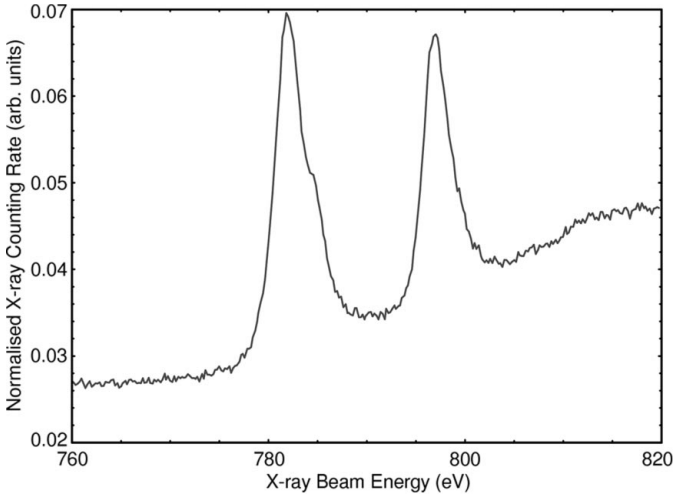

Figure 9
X-ray emission XAS scan over the Co L_3 and Co L_2 edges in Sample-Co.

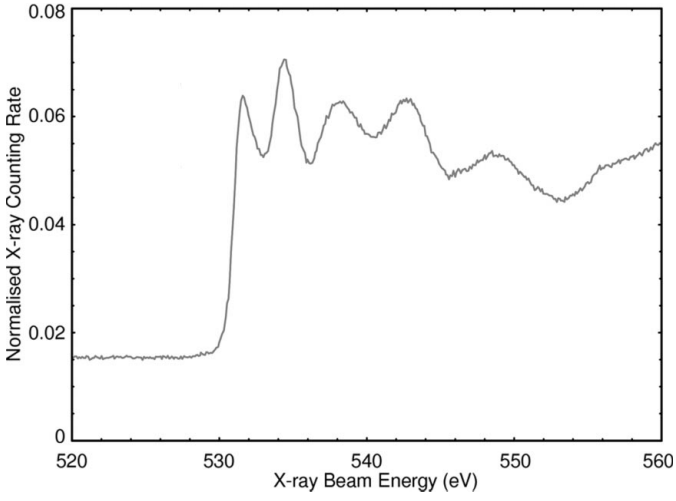

Figure 10
X-ray emission XAS scan over the O K edge in Sample-Co.

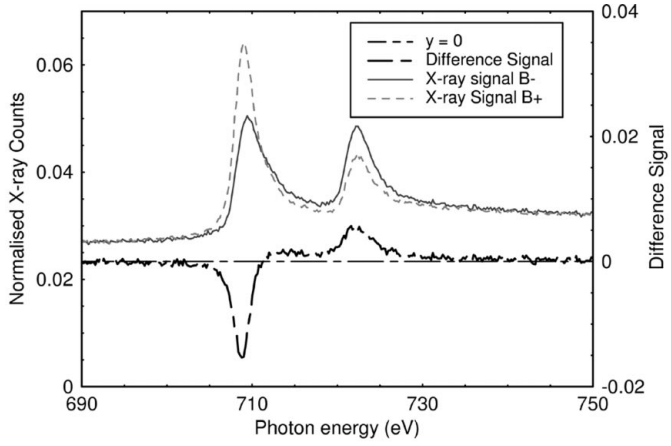

Figure 11
XAS scans over the Fe L edge using Sample-Ga, for each polarity of the magnetic field. Also shown is the dichroism signal, which is the difference between the two XAS scans at a magnetic field of ± 0.5 T. It is noted that no correction other than that for incident flux variations is applied to this data.

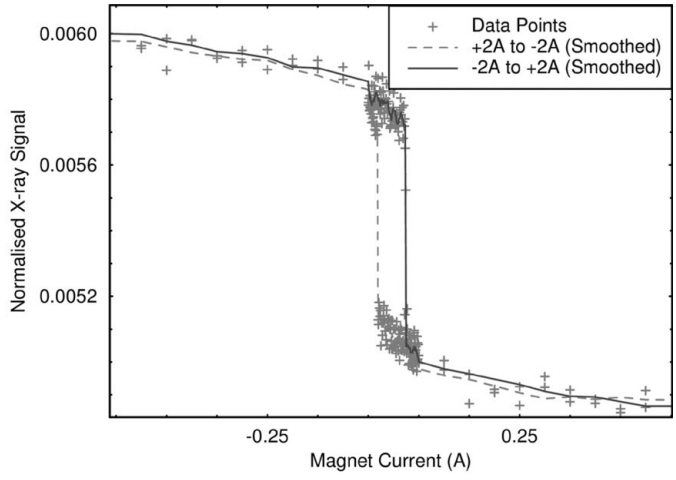

Figure 12
Hysteresis curve taken on the Fe L_3 edge using Sample-Ga. It is noted that no correction other than that for incident flux variations is applied to this data. A current of 2 A corresponds to a magnetic field of 0.5 T. Exposure is 20 s per point.

presented have absolutely no such corrections made, the only adjustment necessary being to normalize the collected data against the incident beam intensity. As corrections rely on assumptions, the fluorescence data are considered to be more reliable. However, they do suffer from the low yield of the fluorescent photon production process, meaning that they suffer from much higher levels of statistical noise (Bateman *et al.*, 2001*b*).

7. Conclusions

The X-ray detector described in this paper is shown to be capable of detecting a variety of X-ray energies in the region 250–1500 eV. This makes it suitable for X-ray absorption experiments involving the transition metal *L* edges and the lighter-element (C, N, O) *K* edges. While flexibility in the filling gas is very useful, the window seriously limits the efficiency of the detector as the energy reduces to near the carbon *K* edge (Fig. 2). At the carbon *K* edge, the step increase in window transmission makes the detector sensitive to carbon K_α X-rays.

The technique of exciting a sample just above and just below an edge of interest, to allow a difference PH spectrum to be calculated, increases the quality of the detector data by removing secondary effects. In combination with the lognormal fitting model, lines can be clearly identified allowing the selection of discriminator window parameters to optimize the signal-to-noise ratio in a scan. Both an upper and lower threshold can be selected, to minimize harmonics and other second-order effects which appear as background in scans, thus maximizing the signal-to-noise ratio for a given experiment.

The GMSD X-ray detector evaluated was housed in a vessel that was designed for magnetic studies. This has resulted in it having to be very small (*i.e* within a 30 mm diameter tube) in order to fit within the magnet being used. The tight space constraints have resulted in a detector that is far from 'wall-less' and has non-ideal drift fields and hence the energy resolution is not as good as it would be in a more ideal detector. A redesigned detector, not constrained by the need to operate in a high-field magnet, would give superior energy resolution [see for example the PH spectra in Fig. 4 of Budtz-Jorgensen (1992)]. The GMSD detector does overcome the limitations of the solid-state detectors listed in the *Introduction*, but even with an improved GMSD this is at the expense of energy resolution.

The high gain available from the GMSD plate used has resulted in a very low noise floor for the device. The 10 Hz noise floor measured for the detector was less than 30 eV. This makes the detector capable of detecting carbon *K*-edge X-rays, opening up the possibility of making fluorescence measurements on biological and other organic substances.

The dichroism and hysteresis scans presented reveal features not previously measured. These should provide the basis for further study. However, the low fluorescence yield of the edges of interest means that count rates in the present beam are very low. The measured flux could be improved either by increasing the exposure time at each point or by increasing the incident flux.

References

Bateman, J. E. (2002*a*). *Nucl. Instrum. Methods*, A**484**, 384–395.
Bateman, J. E. (2002*b*). *Nucl. Instrum. Methods*, A**488**, 610–622.
Bateman, J. E., Derbyshire, G. E., Dudzik, E., van der Laan, G., Lipp, J. D., Smith, A. D. & Stephenson, R. (2001*a*). *Nucl. Instrum. Methods*, A**467**/**468**, 1140–1143.
Bateman, J. E., Derbyshire, G. E., Dudzik, E., van der Laan, G., Lipp, J. D., Smith, A. D. & Stephenson, R. (2001*b*). *J. Synchrotron Rad.* **8**, 1157–1161.
Budtz-Jorgensen, C. (1992). *Rev. Sci. Instrum.* **63**, 648–654.
Dudzik, E., van der Laan, G. & Thompson, S. M. (2000). *Synchrotron Rad. News*, **13**(4), 18.
Fischer, D. A., Colbert, J. & Gland, J. L. (1989). *Rev. Sci. Instrum.* **60**, 1596–1602.
Koningsberger, D. C. & Prins, R. (1998). *X-ray Absorption. Principles, Applications, Techniques of EXAFS, SEXAFS and XANES*. New York: Wiley.
Laan, G. van der & Thole, B. T. (1991). *Phys. Rev. B*, **43**, 13401–13411.
Mir, J. A., Bateman, J. E., Connolly, J. F., Derbyshire, G. E., Duxbury, D. M., Lipp, J. D., Simmons, J. E., Spill, E. J. & Stephenson, R. (2002). *IEEE Trans. Nucl. Sci.* **49**, 894–898.
Oed, A. (1988). *Nucl. Instrum. Methods A*, **263**, 351–359.
Smith, A. D., Bateman, J. E., Derbyshire, G. E., Duxbury, D. M., Lipp, J., Spill, E. J. & Stephenson, R. (2001). *Nucl. Instrum. Methods*, A**467**/**468**, 1136–1139.
Stohr, J. (1992). *NEXAFS Spectroscopy*, *Springer Series in Surface Sciences 25*. Berlin: Springer Verlag.
Veenendaal, M. van, Goedkoop, J. B. & Thole, B. T. (1996). *Phys. Rev. Lett.* **77**, 1508–1511.

 Received 27 May 2003 • Accepted 5 August 2003